Insulating MgO–Al2O3–LDPE nanocomposites for offshore medium-voltage DC cables.

GUPTA, R., SMITH, L., NJUGUNA, J., DEIGHTON, A. and PANCHOLI, K.

2020

Novel Ultra-insulating MgO-Al_2O_3-LDPE Nanocomposites for Offshore High Voltage DC Insulations

Ranjeetkumar Gupta[1], Lindsay Smith[2], James Njuguna[1], Alan Deighton[2], Ketan Pancholi[1]*

[1] School of Engineering, Robert Gordon University, Aberdeen AB10 7GE, UK
[2] Technip Umbilicals Ltd., Research and Development Centre, Newcastle upon Tyne, NE6 3PN, UK

ABSTRACT

Polymer-metal oxide nanocomposite is a key in developing a high temperature insulation material for power electronics and HVDC and MVDC subsea cables having capability of transmitting offshore renewable energy with lower losses and higher reliability. To achieve higher operation voltage level and larger power capacity at reduced cable size, weight and volume, the lighter material offering improved electrical insulation at high operating temperature is required. Addition of metal oxide ceramics in the polymer is shown to improve the insulating properties of the polymer used in the cable and power electronic applications, however, their performance deteriorates at elevated temperature as thermal energy facilitates the electron injection to the bulk material following conduction according Schottky emission. In this work, the heat insulating Al_2O_3 nanoparticles are added to the MgO-polyethylene nanocomposite to observe the effect of interface between mix oxide nanoparticles on current density and breakdown strength of the nanocomposite compared to the MgO-Polyethylene nanocomposite at room and elevated temperature (90°C). The concentration of the MgO and MgO+Al_2O_3 mixture were varied from the 1 wt% to 12 wt% to find out that the nanocomposite containing MgO showed best response than MgO+Al_2O_3 at elevated and room temperature. There is no unified trend was observed in the leakage current density and breakdown strength results for the MgO+Al_2O_3 nanocomposite indicating absence of the interface formation between MgO and Al_2O_3. Decrease in interaction radius, calculated using numerical simulation of nanoparticle dispersion state resulted in the high breakdown strength. Addition of 12 wt% MgO helped achieving highest breakdown strength but overall breakdown strength for MgO+Al_2O_3 nanocomposite improved at elevated temperature.

KEYWORDS: oxide nanoparticles, interface, LDPE dielectric composite, thermal conductivity, extrusion, HVDC insulation, breakdown strength

INTRODUCTION

The capacity of offshore wind parks and subsea oil/gas processing facilities are expanding in size and require improved solutions for reliably transmitting large amounts of electric power using a smart energy system. The core of the upcoming smart energy system demands accelerated improvements in the transmission and distribution capacities of direct current based high voltage (MVDC) cables. With currently available offshore MVDC technology, the cost overruns and maintenance issues are frequent and the reports *(1)* suggest that 80% of wind farm insurance claims in European continent have been cable-related. Development of the material for the long-distance transmission cables is no longer in focus, conversely, the development of materials for MVDC cables has come under intense focus *(2)*.

In the past, various MVDC cable insulation materials have developed to increase the voltage carrying capacity. The paper insulated, oil-filled cable for both AC as well as DC, are capable of serving the voltage up to 800 kV but limited to 80 km length and cross-sections of 3000 mm^2 *(3)*. However, if mass impregnated, non-draining compound (MIND) insulations are used, the length limitations can be overcome but the voltage carrying capacity for the cables of cross-sections up to 2500 mm^2 are limited to 525 kV. These materials face major limitations because of the use of harmful materials such as lead sheath and the impregnation compound *(4)*. To restrict the harmful material use, the cross-linked polyethylene (XLPE) insulation is now used to carry voltage as high as 525 kV with the cross-sections limited to 2500 mm^2 enabling high power transmission capacity at an operating temperature up to 90°C. It offers practically no limitation on length, but it presents a major challenge of harmful gas generation during vulcanisation *(5)*. Alternatively, the high-performance thermoplastic elastomer (polypropylene) (HPTE) insulations are used for medium & 110 kV AC and 320 kV DC transmissions, with operating temperatures as high as 90°C and cross-section 2500 mm^2 *(6)*.

XLPE is a common polymer used as medium voltage (MV) subsea cable insulation material, however, its technological limit has been reached due to the polymer's high energy density and very low thermal conductivity. The current commercial feasibility and development of HVDC/MVDC cables depend on achieving higher operation voltage level and larger power capacity at reduced cable size, weight and volume. An increase of current density, however, results in increased operating temperatures and insufficient electric conduction. Therefore, the new lighter material offering with improved electrical insulation at high operating temperature is required. Additionally, the demand for high-temperature dielectric materials is driven by its potential applications as capacitive energy storage in many power electronics applications such as electric vehicles, aircraft and pulsed power system.

The new insulating material should not allow the formation of electrical treeing and space charge concentration *(7)*, which is a major cause of the complete breakdown, ageing and subsequently, damage to the polymer matrix. Space charges are accumulated electrons/holes and charges (cation or anion) on the surface of the material causing the inhomogeneous distribution of the electric field. Excessive charge accumulation can lead to electric treeing and damage the material. Control the space charge formation is key to the development of the new materials *(8)*. Polyethylene, with a high bandgap, dielectric strength and resistivity, is widely used as an insulating material for the cable. Preparing nanocomposite by adding the metal oxide nanoparticles to the polyethylene matrix can enhance the insulating property by trapping the electrons at the interface of the metal oxide nanoparticles *(9)*. The combinations of polymers and nano-particles, that have already been used as electric cable insulating materials, are graphically summarised in Figure 1, with their dielectric and thermal conductivity values *(10)(11)*. Also, the various electric cable insulating material failure modes are mentioned with their associated causes in Figure 1. Addition of the nanoparticles reduces the problem of field enhancement and space charge accumulation to achieve an extremely low dc conductivity of its insulation.

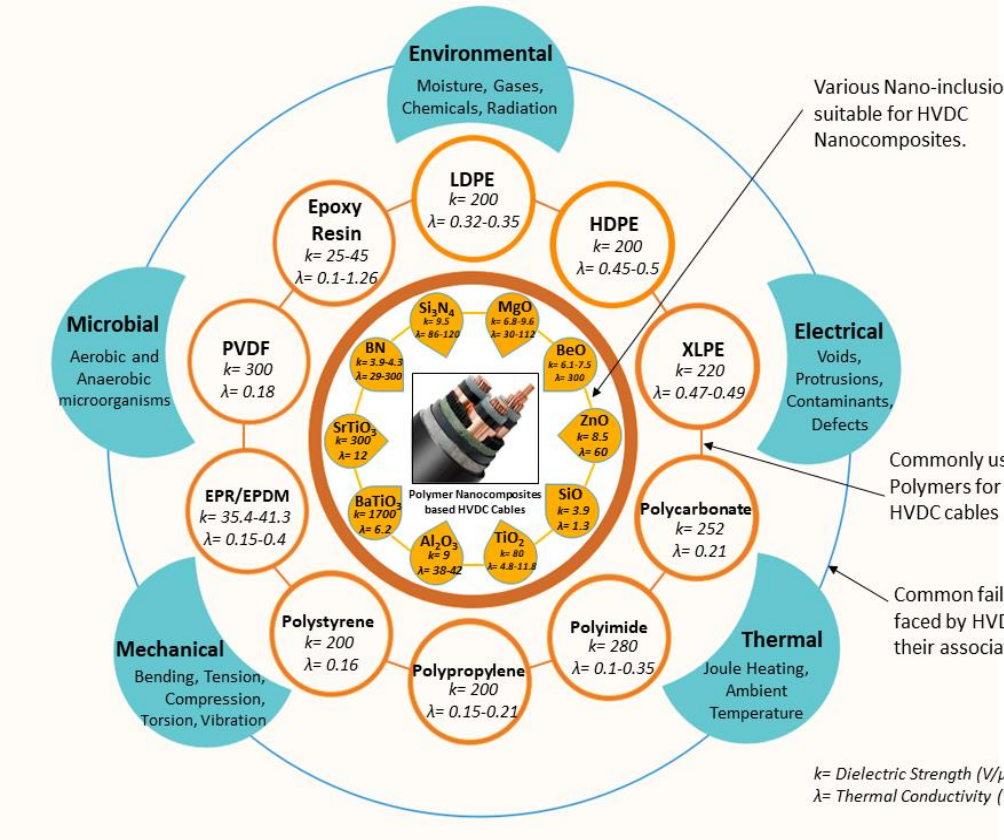

Figure 1. A summary of potential combinations of nano-inclusions and polymers suitable for synthesis of insulating polymer nanocomposite outer layer of the HVDC cables. Associated failure modes of insulating outer layer of the HVDC cables are shown in outermost circle.

Ideal nanoparticles material should have a large bandgap *(12)* with a stable valence state as a cation to decrease the probability of electric conduction. Moreover, these materials also should have high lattice energy to prevent conduction at the high temperature *(13)*. Oxides of Group II and III such as magnesium oxide *(14)*, beryllium oxide *(15)*, zinc oxide *(16)*, silicon dioxide *(17)*, titanium dioxide *(18)* and aluminium oxide *(19)* have been used previously for preparing the insulating polyethylene nanocomposite. However, the mixed metal oxides have not widely been used for preparing the insulating polymer nanocomposite *(20)*. Mixed metal oxides are being used in

electronics applications as they exhibit higher dielectric and ferro-electric properties at elevated temperature than single metal oxide. Magnesium oxide (MgO) and aluminium oxide (Al_2O_3) have been mixed to obtain complete amorphous structure at their interface in the resulting material *(21)*, which can help reducing the loss in dielectric property due to thermally induced electron injection. To observe the change in the electrical insulating properties in relation to mix inorganic nanoparticles present in polyethylene-based nanocomposite, the functionalised MgO and its mixture with Al_2O_3 were used as nanofillers in this work.

Additionally, the chemical composition and a homogenous dispersion of the nanoparticles in the polymer matrix enhance the insulating properties of the nanocomposite. However, it is difficult to quantify the enhancement in the insulating properties of the nanocomposite in relation to the variations in the dispersion state, exfoliation, alignment and aspect ratio of the nanoparticles; just by measuring physical properties of the resulting nanocomposites *(22)*. To correlate the dispersion state and other relevant nanoscale details to insulating property of the nanocomposite, the best part of physical characterisation with simulation intent was combined*(23)*. The dispersion state of nanoparticles in TEM images was used for building the simulated 3-Dimensional (3D) numerical dispersion model, which, subsequently, was used to derive the key parameter of the interaction radius. The interaction radius, representing the average distance of nanoparticles or agglomerates in a 3D space of unit volume of the nanocomposite, influences the conductivity of the designed nanocomposite samples.

Improving dispersion requires the functionalising the nanoparticles *(24)(25)(26)(27)(28)* and therefore, the nanoparticles were functionalised with Trimethoxy(octadecyl)silane. Especially the use of n-Heptane as the solvent for anhydrous coating, prevented any oxide formation and facilitated uniform surface coverage for silane *(9)* without interactions with polar atmospheric substances (CO_2). The hydrophobic coating is as moisture resistant coating which helps improving dispersibility of nanoparticles; hence, aiding the high insulation capacity of the synthesised Low density Polyethylene (LDPE) nanocomposite.

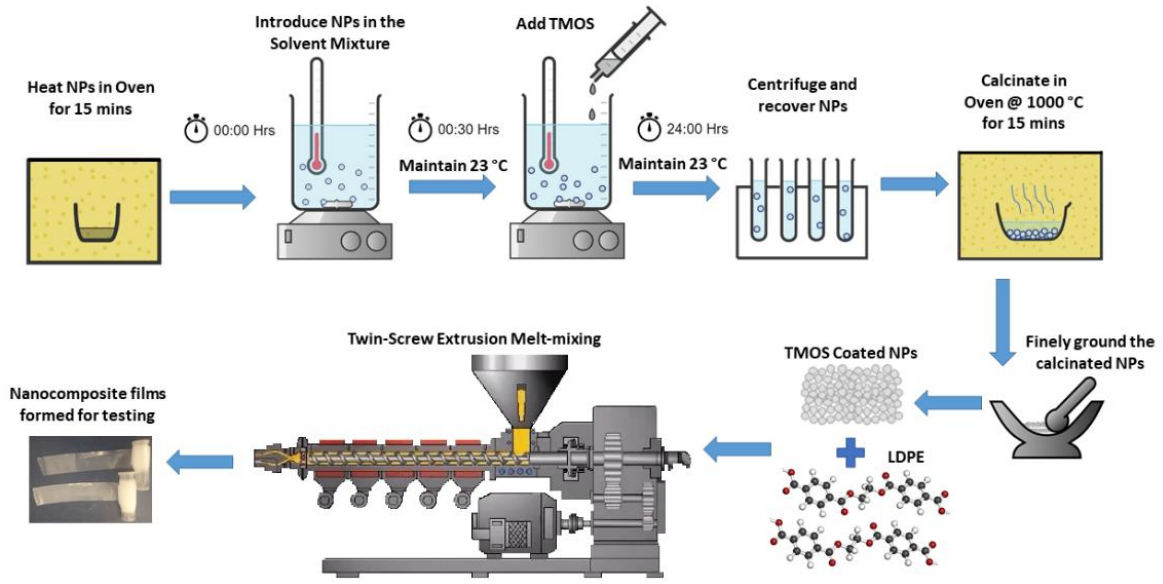

Figure 2. Experimental method followed for the nanoparticle's functionalisation and the subsequent nanocomposite synthesis.

Resulting nanocomposite was tested for its electrical properties to optimise the concentration and dispersion of mix-metal oxide nanoparticles in relation to improvement in the insulating capacity of next generation HVDC cables.

EXPERIMENTAL SECTION

i. Materials.

Magnesium oxide (MgO) nanopowder (< 50 nm size), Aluminium Oxide (Al_2O_3) nanopowder (< 50 nm size), 90% technical grade Trimethoxy(octadecyl)silane (TMOS), Cis-cyclooctene containing 100-200 ppm irganox 1076 FD as antioxidant, 95% and anhydrous 99% Heptane were all used as received from Sigma Aldrich (UK). Low Density Polyethylene (LDPE) granules with 2 g/10 min melt flow rate (920 Kg/m^3) was purchased from Goodfellow (UK). Other laboratory agents were used as standard.

ii. Experimental Methods.

To evaporate the adsorbed moisture, the MgO powder containing nanoparticles were dried in a programmable vacuum evaporator maintained at constant temperature of 550 °C. After the completion of an hour-long drying cycle, the 5 g of MgO nanopowder was then dispersed in 2000 ml of n-Heptane. In the prepared MgO suspension, the 9.15 ml TMOS was gradually added under vigorous stirring and the stirring using a probe type ultra-sonicator was continued for 30 minutes at 100 kHz frequency. Even addition of the small amount of TMOS ensured the functionalisation reaction to proceed as the methoxy groups of C18 carbons are highly reactive. The anhydrous silanisation using n-Heptane mitigate hydrogen bonding and shield polar surfaces from interaction with water by creating a non-polar interphase. Hydroxyl groups can transform MgO into $Mg(OH)_2$ and are the most common sites for hydrogen bonding. The reaction was then allowed to proceed for 24 h at RT, under magnetic bar stirring. The modified MgO nanoparticles were washed three times with n-Heptane and the excess silane was discarded by centrifuging the sample at 2500 rpm in IEC Centra – 4X Centrifuge (International Equipment Company). Finally, the modified MgO nanoparticles were dried in oven at 1000 °C for 10 minutes. Similar method was followed for Al_2O_3 nanoparticles surface-modification. Henceforth, the unmodified MgO and Al_2O_3 nanoparticles will be referred as Un-MgO and Un-Al_2O_3 respectively, whereas the TMOS modified samples will be referred as TMOS-MgO and TMOS-Al_2O_3.

The nanoparticles were analysed for functional groups, especially to distinguish the functional silane coating by preparing into 7mm KBr pellets using the standard mechanical die-set. 0.7-0.8 mg of the nanoparticles were mixed with 2-3 gm of KBr powder and ground together using an agate jar and pestle set. Though homogeneous mixing will give the best results, the excessive grinding is not desired. The prepared mixture was pressed in the die set under vacuum for 7-8 minutes by applying 8 Tonnes load. The pellet was recovered and then set on the KBr holder for FTIR analysis.

The mixture of functionalised nanoparticles and LDPE was melt-blended using the extruder to prepare the nanocomposite. The procedure is summarised and graphically represented in Figure 2. Total four weight (wt) concentrations (1, 3, 6 and 9 wt% of MgO and MgO+ Al_2O_3) of nanoparticles was used to prepare nanocomposites. Firstly, 1 wt% of TMOS-MgO was mixed with 15 gm of LDPE along with 0.5 ml cis-cyclooctene. The cis-cyclooctene prevents the oxidation of the polymer during processing. During the processing, the Twin-tech 10 mm twin-screw extruder temperature was maintained at 140 °C and the screw speed was maintained at 60 rpm. To improve the dispersibility of the nanoparticle, each sample was extruded two times. Resulting films of 80-150 μm thickness were stored for further characterisation. Similarly, 1 wt% samples of TMOS-MgO+Al_2O_3 (having 1:1 wt% ratio of each of the nanoparticles) along with the samples with different wt% (3, 9 and 12 wt% of nanoparticles) were synthesised.

iii. Characterisation Techniques.

Attenuated Total Reflection spectra (ATR-FTIR) were recorded on Perkin-Elmer make, using DGS-KBr sensor for identifying the effect silane functionalisation of nanoparticles. Nanocomposite films of thickness around 80-150 μm thickness were prepared and a total of 30 scans in the range of 525–4000 cm^{-1} wavenumber was carried out to identify functional groups and structural changes after the addition of nanoparticles, at a resolution of $4cm^{-1}$.

For analysing the surface characteristics of the functionalised nanoparticles and the dispersion-pattern of nanoparticles in the LDPE matrix TEM images were taken. Nanoparticles were dissolved in ethanol and a tiny drop was taken from this solution on the copper grid and left for natural drying, as forced drying can bring the nanoparticles together as clumps. Ultrathin section of the nanocomposite was obtained by microtome and placed on 400-mesh-size gilder copper grid. The images were then captured on Philips CM100 TEM with an accelerating voltage of 100 kV and a spot size of 10 nm, with 0-50 s exposure time. The magnification range of x7900 to x245,000 was used to capture images.

Differential scanning calorimetry (DSC) and Thermogravimetric analysis (TGA) was performed using TA Instruments DSC Q100 and TGA Q500 using a sample mass of 7-12 mg. For DSC, Heat/Cool/Heat standard cycle type analysis was selected for accurately depicting the behaviour and T_m for the samples prepared. The running segment consisted of a ramp heating at 10 °C/min from 25 to 150 °C, then ramp cooling at 5 °C/min to -50 °C and finally ramp heating at 10 °C/min to 150 °C. In TGA the heating rate was 10 °C/min and the 100% weight reduction mode was selected for the analysis. Detailed crystallisation calculation method is discussed in Supporting Information S1.

Thin films with thickness of around 200 ± 10μm were used for measurements but the direct current (DC) electric field applied was for unit millimetre. Both the top and bottom surfaces of the samples were deposited with copper electrode of the diameter of 7 mm. The current data were collected under the applied alternating electric fields up to 60 kV/mm to obtain current vs applied electric field characterisation. The maximum applied field was 116.85 kV/mm. All the measurement was performed at room temperature and 90°C.

Breakdown measurement was carried out by applying high DC electric field via the pin type electrodes (7 mm in diameter, Brass material) and the electrode system with sample was immersed in the pure silicone oil during the measurement. An electric field was applied until the sample was broken down. The electric field increases proportional to the thickness of film. This makes results obtained with any film any thickness comparable. In other word, the applied field was independent of thickness. For every sample, five specimens were used to obtain all the data.

iv. Simulated model generation.

The TEM micrographs were used as an input for building the simulated 3D model using MATLAB® platform. The micrographs were processed in Photoshop® software; wherein they were cropped, rotated and enlarged, for removing their edges and any distorted background. Further, they were digitally enhanced using filters for the several purposes such as removing the background noise and their artefacts or improving upon the definition and sharpness of the image. All grayscale images were corrected for the brightness and contrast to achieve correct black and white tonalities, which helped distinguishing the polymer matrix represented by the grayscale region and the pure black entities representing the nanoparticles. Finally, the polymer background images were toned with the yellow and green colour and the black nanoparticle entities toned with red and black colour representing MgO and Al_2O_3 nanoparticles/agglomerates, respectively. The red and black toning of nanoparticles/agglomerates were random in nature as they were trivial to the study. Then the final toned images were saved as high quality 8-bit TIFF format and loaded in ImageJ image processing software for estimating the nanoparticles/agglomerates sizes of all the sample variations. This size data was then added as input to the bespoke designed MATLAB® code, to be used as a basis for generating the random nanoparticles/agglomerates in the simulated 3D model of the nanocomposite. The code was able to generate the model with the required concentration of nanoparticles and sizes within the input diameter range. Same image tone colours were allocated in in the simulated model as well, where the red and black colours were representing MgO and Al_2O_3 nanoparticles/agglomerates, respectively.

Results and discussion

i. Evaluation of functionalisation of nanoparticles.

The FTIR spectrum for the uncoated (Un-MgO and Un-Al_2O_3) and coated (TMOS-MgO and TMOS-MgO+Al_2O_3) nanoparticles are presented in Figure 3. The sharp peaks at 1057 and 1058 cm^{-1} confirmed the formation of Si–O–Si bonds or those relevant to Si-O-R where R is being an associated alkyl unit *(29)*. Slight peak shoulder is formed at around 3717 cm^{-1} and 3720 cm^{-1} due to the condensed silanes, but it seems mostly suppressed by the broad peak between 3750-3200 cm^{-1} viz. due to the proton donors in surface hydrogen bonds attributed by the surface -OH groups. The stretching around 3750-3710 cm^{-1} related with multi-coordinated surface and isolated –OH groups has also been reported as dependent on the exposed crystal surface of metal oxide nanoparticles *(30)*.

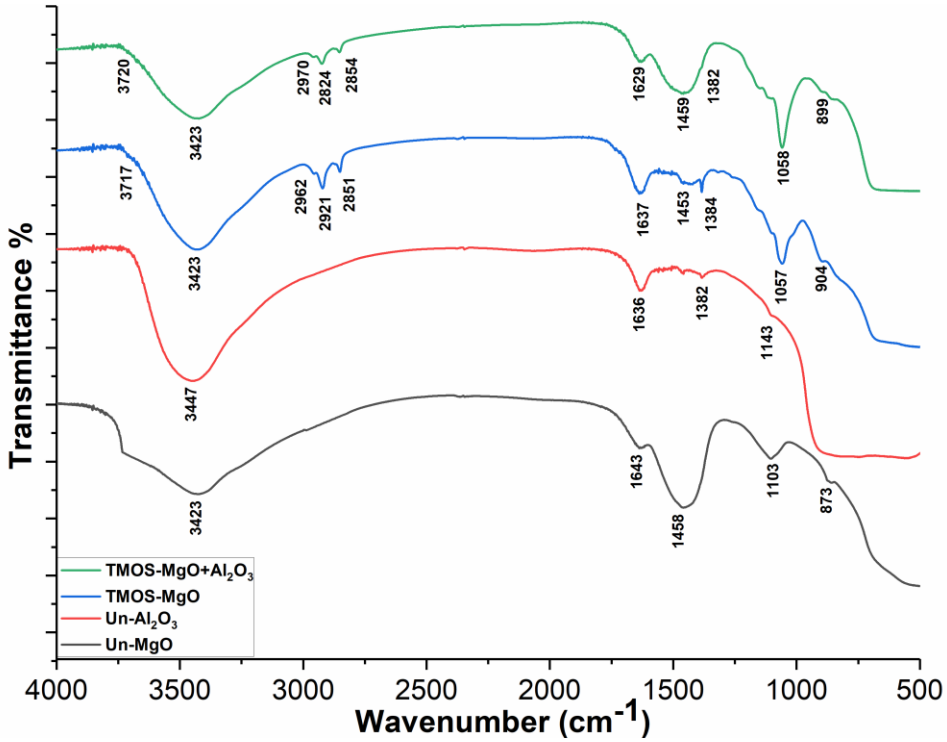

Figure 3. IR Spectra of the Uncoated (Un-MgO and Un-Al_2O_3) and Coated (TMOS-MgO and TMOS-MgO+Al_2O_3) nanoparticles.

Chemisorption of CO_2 on surface of the nanoparticles forms a bidentate carbonate (O–C–O) with single or double bridging bonds and appears as a hump of broad peak at 1458 cm^{-1} while enveloping the 1700-1300 cm^{-1} range *(31)(32)*. Similar intensity of peak for the chemisorbed CO_2 from the atmospheric air contamination of the nanoparticles has been reported earlier *(33)*. The peaks observed at 1458 and 1643 cm^{-1} for the Un-MgO nanoparticles attributed to CO_2 and H_2O adsorption respectively, are considerably suppressed in the coated nanoparticles, indicating better steric hindrance for adsorption of TMOS *(31, 32)*. On contrast the Un-MgO nanoparticles showed greater extent of adsorbed surface water as seen with the broad peak around 3200-3750 cm^{-1} and another at 1643 cm^{-1}. During the surface modification of nanoparticles this surface water was utilised to facilitate the hydrolysis of silane, hence the limited water content in the coated nanoparticles.

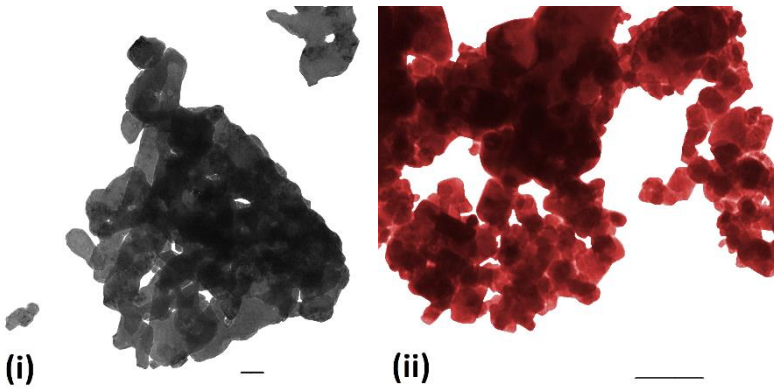

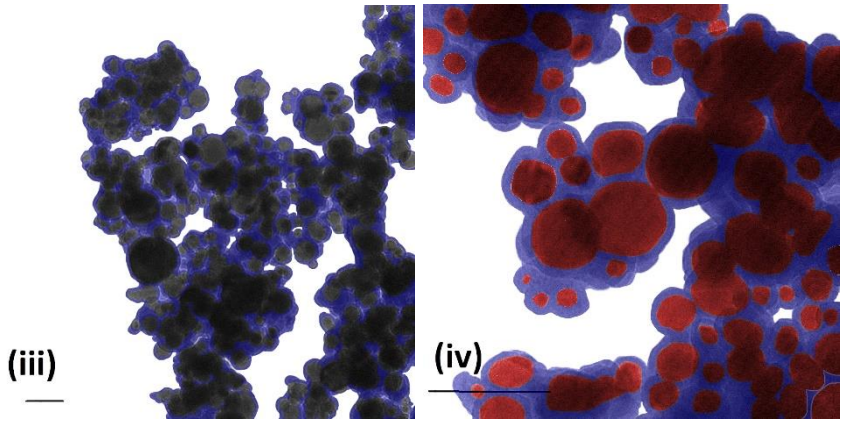

Figure 4. Processed TEM images of uncoated [(i) Un-MgO & (ii) Un-Al_2O_3] and coated [(iii) TMOS-MgO & (iv) TMOS-MgO+Al_2O_3] nanoparticles. (Wherein, MgO is assigned as black and Al_2O_3 as red particles respectively, and the Bar Scale marked is of 100 nm)

The high-resolution TEM images of the nanoparticles before and after the TMOS functionalisation process were taken to analyse the effect of the silane coating on the nanoparticles surface and eventually their behaviour on the dispersion in the LDPE matrix. As seen in Figure 4, the original TEM images (original TEM images are included in Supporting Information S2) are processed to assess the functionalisation effect on the nanoparticles surface. The Figure 4 (i) & (ii) show the uncoated nanoparticles that were clumped together due to the adsorption of atmospheric moisture and gas (H_2O and CO_2). The agglomerating tendency was greatly restricted after application of the silane coating on the nanoparticles surfaces, as it is evident from the Figure 4 (iii) & (iv). These images show the well separated nanoparticles with the thickness of the shell layer of these surface-treated nanoparticles was found to be approximately 8-18 nm. The thickness measurements were made using ImageJ.

ii. Effect of variations of nanoparticle concentration

IR spectra in Figure 5 show the LDPE related peaks of -CH_2 stretching band around 2911-2916 cm^{-1} and the -CH_3 stretching band around 2839-2849 cm^{-1} (marked with 'Δ' notation), however, these peaks are suppressed the presence of alkyl group from the Trimethoxy(octadecyl)silane coating as was observed in Figure 3. The other representative LDPE peaks of ν(C=O), δ(C-H), γ(=C-H) and γ(C-H) is subsequently seen at around 1450 cm^{-1}, 1460 cm^{-1}, 1030 cm^{-1} and 710 cm^{-1} and are marked with the notations of Θ, Γ, ϑ and o, respectively. All the spectra of the various samples are much similar in nature, with a residual broad peak at about 1453-1469 cm^{-1}. On the slope up to the NP-bulk absorption (709-725 cm^{-1}) *(31)*, the small peaks at 714-719 cm^{-1} (TMOS-MgO) and 709-725 cm^{-1} (TMOS-MgO+Al_2O_3) have been attributed to Si–O stretching in the SiOH *(29)*, while the peak at 862 cm^{-1} was assigned to OH from the adsorbed H_2O *(32)*. Mild suppressions of peak at around 3550 cm^{-1} marked as Ψ is due to the low presence of the hydroxyl bond associated with the moisture adsorption on the MgO nanoparticle surface. Low adsorption was observed due to silane coating and the effect of this suppression is clearly visible in the Figure 3 & 5. All peaks associated with the nanoparticles of MgO and Al_2O_3 are accordingly marked in the Figure 5 with the notations θ and Φ & φ respectively *(24)(25)*. The peak related to Si-O-Si bond formation observed around 1038-1053 cm^{-1} (Figure 3) in nanoparticles spectra appears sharp compared to the same peaks observed in the nanocomposite spectra. The suppression of the peak related to the Si-O-Si bond formation in the nanocomposite spectra can be attributed to presence of LDPE matrix. The peak is marked with π notation in Figure 5.

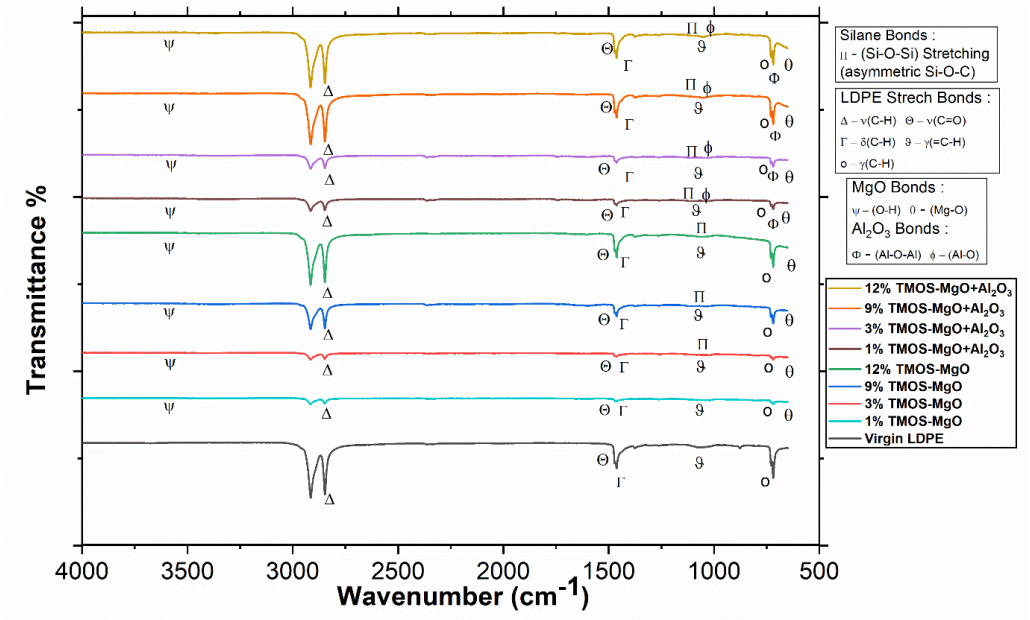

Figure 5. IR Spectra of the LDPE nanocomposite containing varying concentrations (in wt%) of coated and uncoated nanoparticles. The black trace represents an IR spectrum of the Virgin LDPE.

The DSC analysis is an important tool for discriminating the mechanical and thermal stability of a sample based on the transitions of the physical properties involving heat flow; as the degree of crystallinity will dictate the suitability of the synthesised nanocomposite for structurally sound application *(27)*. The analysis is done to quantify the endothermic transition energy absorbed during the melting phenomenon and the exothermic crystallisation energy released whilst the cooling down of melted sample. The samples showed variation in heat absorbed during melting, as associated with the crystalline lamellae transforming into viscous amorphous structure; this variation depends on the range in crystal sizes and defects within the crystals. The decreasing trend of the melting temperature (T_m) and the associated increase in melting range of both the variations of samples i.e. with TMOS-MgO and TMOS-MgO+Al_2O_3 with the increasing concentration of the nanoparticles, as is expected with increasing impurity level in the sample *(34)*. Further the degree of crystallinity of all the samples was calculated with standard procedure using the melting heat of 286.7 J/g of completely crystallised polyethylene *(35)* (calculation method listed in detail in the Supporting Information S1) and are shown in Table 1.

Table 1. A list of Melting temperature (T_m), Crystallization temperature (T_c)and degree of crystallinity from DSC results.

Sample	T_m (°C)	T_c (°C)	Enthalpy (J/g)	Degree of Crystallinity (%)
Virgin LDPE	109.46 ± 1	98.37 ± 1	110.46 ± 1	38.53 ± 1
1% TMOS-MgO	110.89 ± 1	98.66 ± 2	110.12 ± 2	38.41 ± 2
3% TMOS-MgO	110.78 ± 1	98.59 ± 2	109.81 ± 2	38.30 ± 2
9% TMOS-MgO	110.26 ± 2	98.22 ± 2	98.74 ± 2	34.44 ± 2
12% TMOS-MgO	109.89 ± 1	98.16 ± 2	96.11 ± 3	33.52 ± 3
1% TMOS-MgO+Al2O3	110.28 ± 2	98.98 ± 1	110.09 ± 1	38.40 ± 1
3% TMOS-MgO+Al_2O_3	110.11 ± 2	98.97 ± 1	109.00 ± 1	38.02 ± 1
9% TMOS-MgO+Al_2O_3	110.01 ± 1	98.95 ± 2	99.55 ± 1	34.72 ± 1
12% TMOS-MgO+Al_2O_3	109.54 ± 1	98.92 ± 1	98.59 ± 1	34.39 ± 1

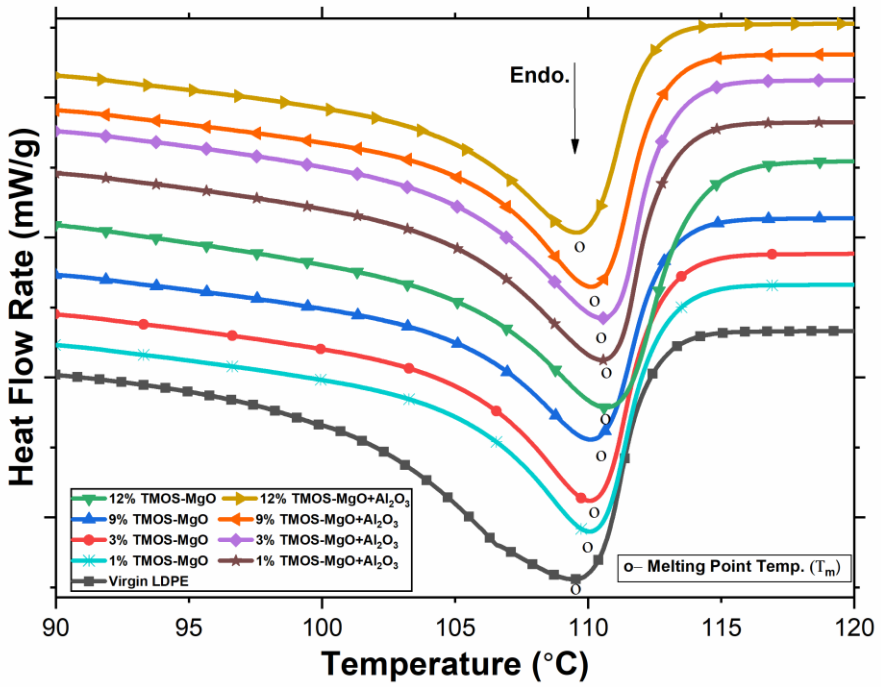

Figure 6. DSC melting endothermic peaks used for crystallinity calculation for all the nanocomposite samples prepared, and its comparison with that of the Virgin LDPE. (Endo. represents Endothermic process)

Figure 6 show the DSC curves for the heating (taken at 10 °C min^{-1}) whereas Figure 7 represents the cooling curves (taken at 5 °C min^{-1}) for all the nanocomposite samples including virgin LDPE. As seen in Table 1 and Figure 6, the onset temperature of the melting has decreased by *ca*. 1-2 °C for the sample with highest loading of the TMOS-MgO and TMOS-MgO+Al_2O_3 nanoparticles; whereas the crystallisation temperature (Figure 7) increased very slightly by *ca*. 0.5 °C for the TMOS-MgO samples only. In case of the nanocomposite with TMOS-MgO+Al_2O_3 nanoparticles, there is no change observed. The shift in the onset temperature of crystallisation is distinguishingly seen by a slight elevation for all nanocomposite samples compared to Virgin LDPE. With the increasing concentration of nanoparticles of TMOS-MgO, the decrease in onset of melting/crystallisation is evident for all samples except 12 wt%, however, the decreasing trend is observed for all samples with increasing amount of TMOS-MgO+Al_2O_3 nanoparticles concentrations.

This concludes that the nano-inclusions formed nucleating sites, hence reducing the degree of crystallinity with the increase in wt% as observed in other studies on polyolefins *(34)* and also resulting in the subsequent reduction in melting temperature (T_m) and the crystallisation temperature (T_c) *(34)*. However, it is not clearly evident for samples with 12 wt% concentration as the high concentration may lead to agglomeration and uneven heating during the DSC characterisation.

Earlier studies mention that, attaching stearates/coating to metal oxide-type nucleating agents will further attenuate the nucleating activity *(34)*. Which can explain the nucleation due to nanoparticles inclusion in the LDPE matrix.

This crystallinity study suggests that the properties in terms of onset crystallisation and melting of the 12 wt% TMOS-MgO+Al_2O_3 sample is almost matching with the Virgin LDPE, however, TMOS-MgO+Al_2O_3 sample shows lower degree of crystallinity. The effect of this crystalline phase nature is understood to not affect the conductivity directly *(9)*, but the effect with the nanoparticle concentration and type does, which is further investigated in the electrical measurements.

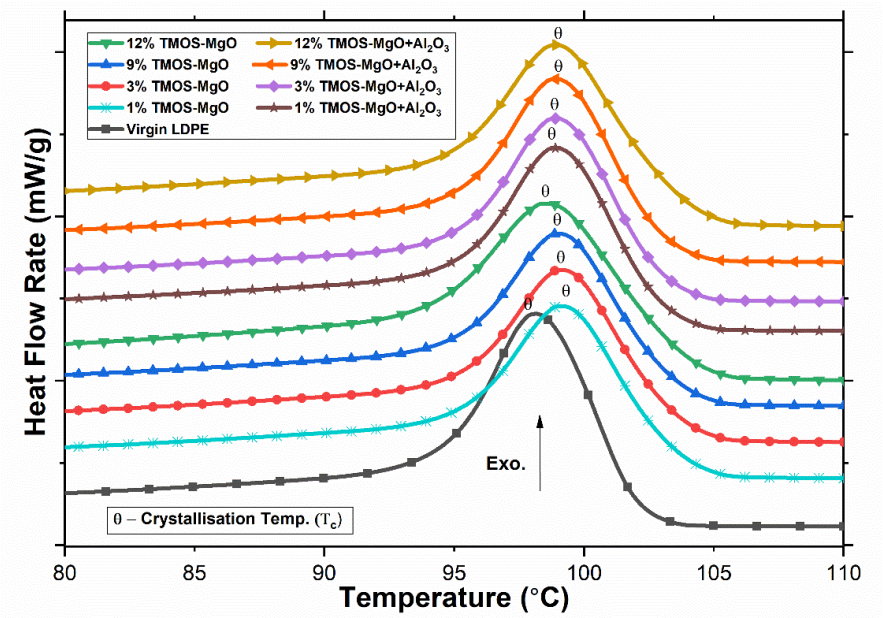

Figure 7. DSC exothermic crystallisation peaks for all the nanocomposite samples prepared, and its comparison with that of the Virgin LDPE. (Exo. represents Exothermic process)

Though the degree of crystallinity decreased with the increasing concentration of nanoparticles for both the sample types, but it also improved the thermal stability of the composites due to the improved dispersion as a result of the silane functionalisation. Figure 8 shows the thermal degradation behaviour of all the samples and compared with that of the virgin LDPE. The virgin LDPE showed the onset of degradation well earlier at a temperature *ca.* 170 °C, as seen in Figure 8. Conversely, the samples with the smallest content of nanoparticles (i.e. 1 wt%) showed an onset temperature at least *ca.* 100 °C higher than the virgin sample; this is obvious due to the nature of the metal oxide inclusions. Also, the increase in the loading of the nanoparticles gradually improved the onset temperature of the samples, but of all the samples the 9 wt% and the 12 wt% TMOS-MgO+Al_2O_3 samples showed the highest temperature for onset of degradation. It is, therefore, attributed to the increased nanoparticle concentration and type of nanoparticles. As seen in Figure 8, the addition of mixture of MgO and Al_2O_3 increases the degradation temperature compared to nanocomposite having MgO only. The heat-stabilising effect is associated with the restricted oxygen accessibility with the possible adsorption of volatile species at the onset of degradation *(36)*.

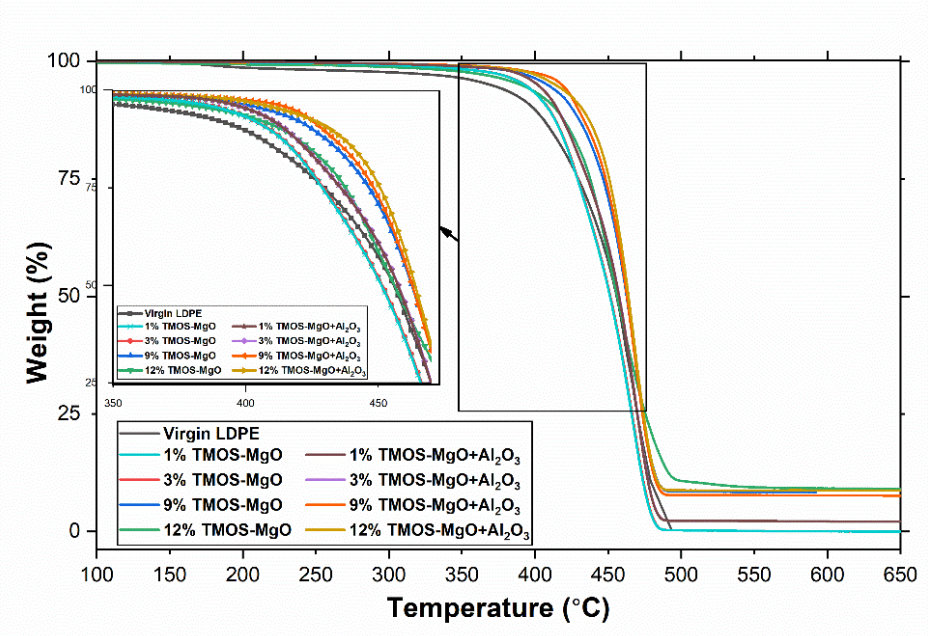

Figure 8. The thermogravimetric analysis (TGA) data plots for all the nanocomposite samples prepared, and its comparison with that of the Virgin LDPE.

iii. Simulated model generation showing interaction radius (IR)

The original TEM micrographs (included in Supporting Information S2) of all the samples, processed as per the methodology discussed in the earlier section, are presented in the Figure 9. As seen in the Figure 9, the agglomeration of the nanoparticles increases with the increase in the nanoparticle concentration, however, the size of agglomerates do not change significantly at highest concentration. As the nanoparticles comes closer with each other in high concentration nanocomposite, the dipole-dipole interaction causes them to agglomerate. Interestingly, the samples with both MgO and Al_2O_3 nanoparticles, showed higher agglomerate sizes which indirectly indicate that Al_2O_3 have higher tendency of forming agglomerate, as compared to the MgO. These images were analysed using ImageJ image processing software and the ferret diameter measurement tool, which approximates each selected region of nanoparticle/agglomerate as an ellipsoidal entity, was used to calculate the agglomerate diameter based on relation $\sqrt{(minFeret \times maxFeret)}$. Final estimated diameter data from this calculation for each sample are summarised in Table 2. The values in Table 2 were then used as an input diameter range for bespoke MATLAB® code to generate the spherical nanoparticles in the simulated 3D model.

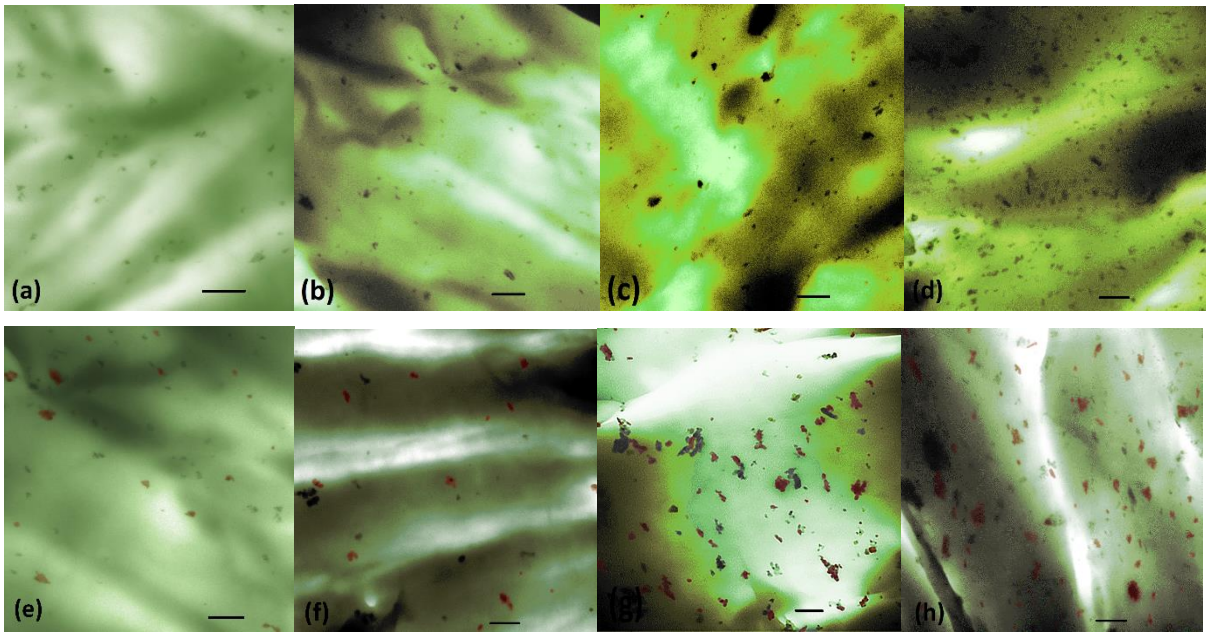

Figure 9. The processed TEM micrograph images for samples with MgO variations [(a) 1 wt%, (b) 3 wt%, (c) 9 wt% and (d) 12 wt%] and MgO+Al_2O_3 variations [(e) 1 wt%, (f) 3 wt%, (g) 9 wt% and (h) 12 wt%] of nanoparticles respectively. (Scale bar represents 500 nm)

Table 2. Estimated ferret diameters of nanoparticle/agglomerate regions identified from TEM micrographs and calculated in ImageJ

Sample	Biggest agglomerate size (nm)	Smallest nanoparticle/ agglomerate size (nm)
1% TMOS-MgO	130 ± 15	30 ± 5
3% TMOS-MgO	115 ± 15	30 ± 5
9% TMOS-MgO	135 ± 10	30 ± 5
12% TMOS-MgO	170 ± 25	30 ± 5
1% TMOS-MgO+Al_2O_3	160 ± 20	30 ± 5
3% TMOS-MgO+Al_2O_3	155 ± 20	30 ± 5
9% TMOS-MgO+Al_2O_3	190± 15	30 ± 5
12% TMOS-MgO+Al_2O_3	220 ± 20	30 ± 10

To keep the complexity of the simulated model to a minimum, all the entities are generated as spherical nanoparticles/agglomerates. The simulated models for all the samples are shown in Supporting Information S3. Wherein smallest spheres represent the individual nanoparticles and the large spheres correspond to agglomerates.

The purpose of the simulated modelling is to visualise and interpret the dispersion state of the synthesised samples with variable concentration of the nanoparticles, which is quite challenging to attain with the physical methods of sample characterisation. Using the distance between the nearest neighbours (spheres) in a simulated volume of the nanocomposite, the interaction radius (IR) of each nanoparticle/agglomerate region were calculated. The IR values for each region containing the individual sphere of variable sizes (Supporting Information S3) helped determine the influencing region or the interaction region of each nanoparticle or agglomerates in the simulated model. The dispersion state and IR are two main parameters that dictate the transfer of charged electrons or conductivity/insulating properties of the synthesised sample *(9)* and therefore, the dispersion sate of the nanoparticles in the nanocomposite was simulated. The values of the IR generated by the bespoke MATLAB® code is summarised in Supporting Information S3, and this data was used for graphically representing the interaction region as shown in Figure 10. Finally, this data is correlated with the measured insulating properties of all nanocomposite samples.

According to the definition, the variable IR values are dependent on the size of the nanoparticle/agglomerate and its nearest neighbours. The IR values are found to be decreasing from ca. 140 nm to 70 nm with increase in the concentration of nanoparticles in nanocomposite. Though having the largest sized agglomerates (as summarised in Supporting Information S3), the sample having both MgO+Al_2O_3 and 12 wt% nanoparticles showed the lowest IR value. This is due to one of the reasons of bigger agglomerates present, as listed previously. Hence, the presence of little higher sized agglomerates present in this sample, is in fact aiding the conductivity performance and viz. confirmed in conductivity measurements later.

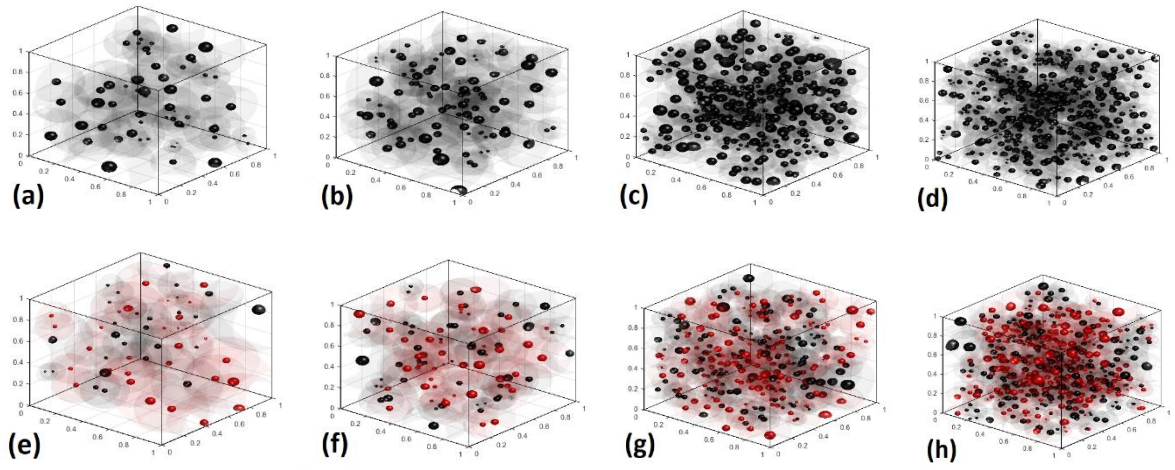

Figure 10. Simulated representation included with the interaction radius (IR) of the individual nanoparticle/agglomerate regions present in the synthesised nanocomposite (1 cubic micron size) for MgO variations [(a) 1 wt%, (b) 3 wt%, (c) 9 wt% and (d) 12 wt%] and MgO+Al_2O_3 variations [(e) 1 wt%, (f) 3 wt%, (g) 9 wt% and (h) 12 wt%] of nanoparticles respectively. (Herein, solid Black spheres represent MgO and Red spheres are for Al_2O_3 nanoparticle or agglomerates and the faint black and red region/sphere around nanoparticle or agglomerates represents their interaction range respectively.)

iv. Electric leakage and breakdown measurement

The electric current leakage density was measured for LDPE and all nanocomposite thin films (80 μm). Measuring the leakage current values provides understanding of the insulating properties of the all materials. Figure 11 shows the values of leakage current density J in response to the applied electric field (E) for all the samples at room temperature.

As seen in Figure 11, the highest current density is observed in the pure LDPE samples subjected to a range of the electric field at room temperature and 90º C. Increasing the concentration of the TMOS-MgO in nanocomposite decreases the leakage current density and improves the insulating property. The 1wt% TMOS-MgO nanocomposite showed highest current density in comparison to all other nanocomposite containing TMOS-MgO. However, all nanocomposite samples containing TMOS - MgO +Al_2O_3 show higher leakage current density at room temperature than that of all TMSO-MgO nanocomposites.

It was reported that charge carriers in O– states were dissociated from the O_2– sublattice of MgO in the bulk and diffused to the surface during the heat treatment with Al_2O_3. After fast cooling of MgO nanoparticles to room

temperature, the charge carriers mainly remained at cation vacancies on the crystal surfaces, which increased the electrical conductivity of the MgO phase *(21)*. On the other hand, the MgO nanoparticles alone in an LDPE matrix act as additional charge traps and increase the space charge barriers thus reducing the charge mobility and DC conductivity within the LDPE matrix. At higher temperature, the O– states return to MgO and increases slightly the resistivity.

However, there is a limit to the loading MgO nanoparticles to reduce the conductivity of pristine LDPE. The increase in loading of nanoparticles improved the insulating properties but it is recommended to reduce loading to retain polymeric properties.

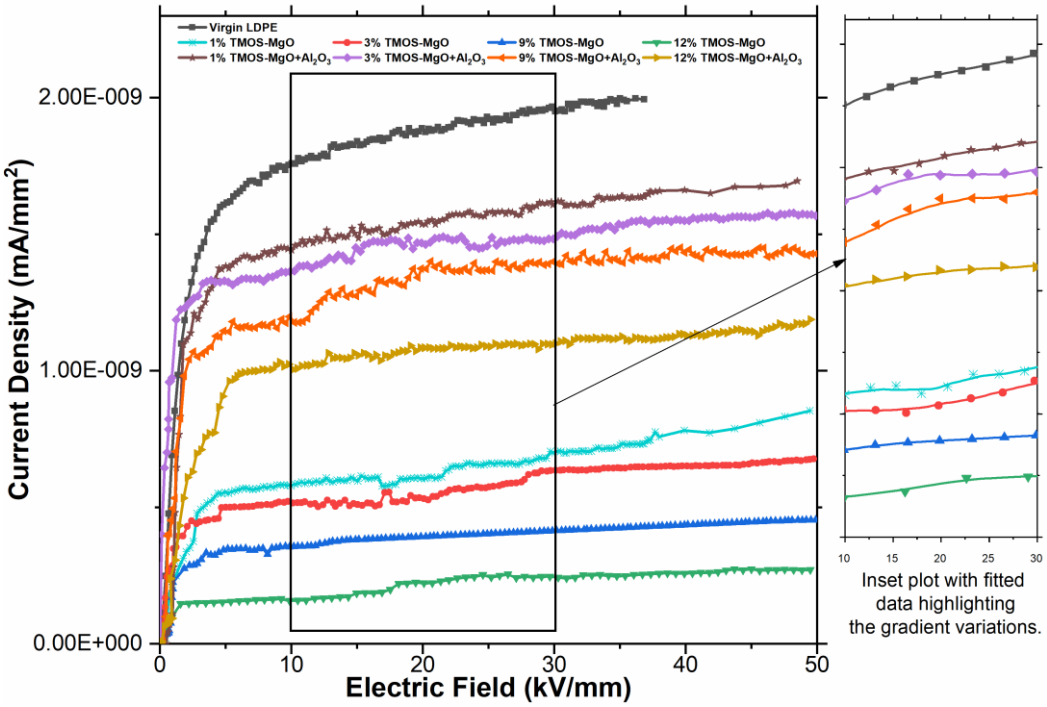

Figure 11. Measured leakage current density for prepared film samples at room temperature.

With small increase in the applied electric field, the value of current density increased rapidly. However, the increase in current density gradient slowed down. It is important to note that the leakage current density data for electric field almost near to breakdown values have not been plotted. The gradient of the curve is quite steep for the values more than maximum electric field showed in Figure 11, however, they were not included in the Figure 11 because measurements for the electric field near breakdown values may affect the sensitive ammeter. However, it is quite evident that the current density changed nonlinearly with the increase in the applied field. First the large increase in current density for electric values <5 kV/mm can be attributed to the space charge accumulation between the electrode and copper film deposited on the nanocomposite film *(37)*. After further increase in the electric field values, the charge trapping at the interface of the nanoparticles and polymer initiated causing considerable reduction in the gradient. Moreover, it is observed that the gradient values for the nanocomposite with high concentration nanoparticles is lower than the nanocomposite with low concentration. Above the electric field of 5 kV/mm, the current density and therefore, the space charge behaviour changed from linear to nonlinear. The electric field where transition occurs is referred as space charge accumulation threshold. The threshold field is found to be reducing with the increase in the nanoparticle concentration in the nanocomposites, which shows the reduction in probability of space charge accumulation in nanocomposite with high concentration of nanoparticles. At higher fields, the space charge accumulation may be dominated by the bulk processes and could be attributed to larger availability of ionic carriers during processing of nanocomposites *(38)*.

For the nanocomposites, the total leakage current density decreases and exhibits the higher breakdown strength (Supporting Information S4). This indicates that the space charge accumulation is suppressed by the capture of injected charges either by deep trapping or charge hopping *(39)*. The current density curves indicate the minor role of the carrier injection at the electrode contacts *(40)*. Considering the plot, it can be deduced that the charge

hopping is taking place and follows the relation for the hopping conduction current in the dielectrics *(41) (42).* The breakdown strength of material was measured separately from the conductivity experiment. Therefore, the maximum field strength used in current leakage measurements do not reflect the breakdown strength of the material. The breakdown strength (Supporting Information S4) of the materials at room temperature showed similar trend as leakage current density. The nanocomposite with 12% MgO was found to show highest breakdown strength.

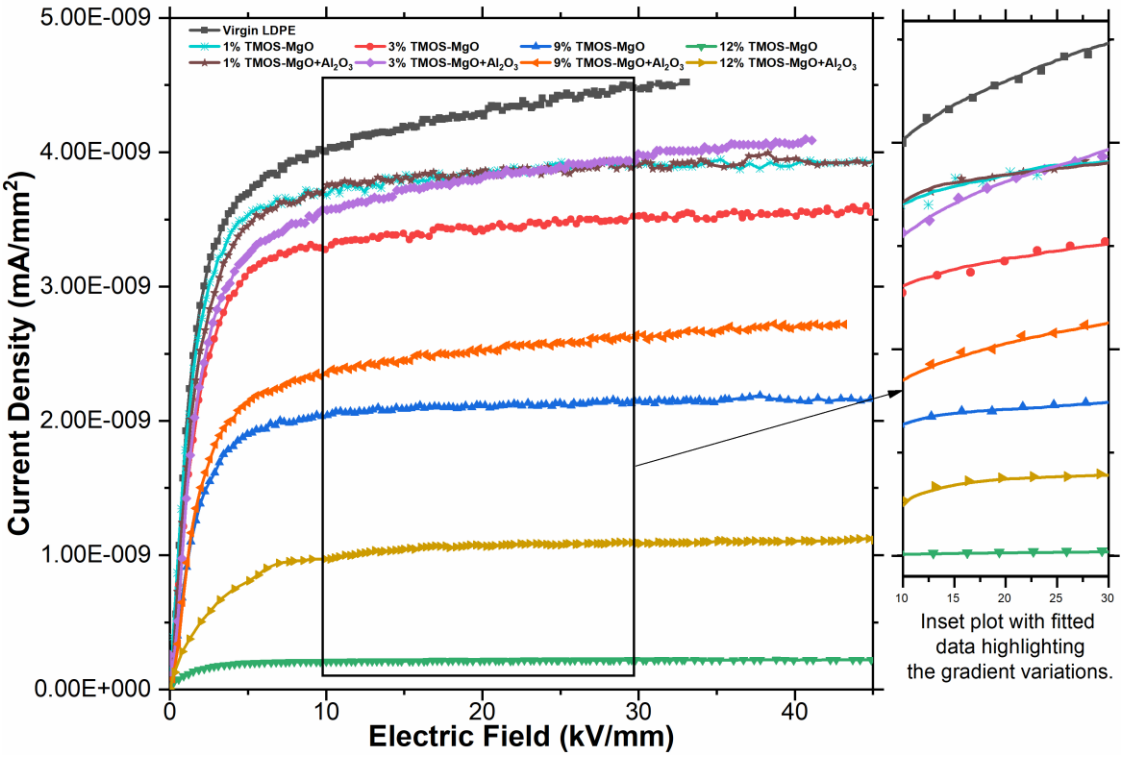

Figure 12. Measured leakage current density through prepared film samples when subjected to electric field at 90°C

Elevated temperature measurement (90°C) was carried out to characterise the suitability of a new material at extreme conditions arising due to extreme heating at high current. The current density in relation to applied electric field at elevated temperature is measured and shown in Figure 1212. Both films containing 1wt% TM0S-MgO and TMOS- MgO+Al_2O_3 shows almost same behaviour at higher temperature which suggest that the charge trapping at low concentration does not change with addition of the Al_2O_3. An interface formation between dielectric insulating with high thermal conductivity ceramics such as Al_2O_3 can improve the dielectric performance at high temperature *(43)*. However, the homogeneity of the nanoparticles at low concentration could be low.

As seen in the Figure 12, the leakage current density of the all materials was increased and insulating properties was affected at elevated temperature. All nanocomposite samples showed less leakage current density than LDPE at 90°C *(44)*. Also, it was worth noting that, at 90°C, both 12% TMOS-MgO and 12% TMOS-MgO+Al_2O_3 showed higher current density than the current density measured at the room temperature. Also, the breakdown strength of 12% TMOS-MgO+Al_2O_3 sample increased at elevated temperature measurement, as compared to the MgO samples which showed a decreasing trend. It suggests that the addition of Al_2O_3 have improved the charge-discharge cycle at the MgO- Al_2O_3 interface *(44)* leading to reduction in space charge injection at higher temperature.

The TMOS-MgO+Al_2O_3 results showed inconsistent pattern. The 12% TMOS-MgO+Al_2O_3 sample performed well at elevated temperature, but the samples with lower weight percentage loading of TMOS-MgO+Al_2O_3 did not show better results as compared with the TMOS-MgO samples. Probably, the inadequate dispersion of MgO and Al_2O_3 nanoparticles at the 3% and 9% loadings would have not provided consistent results. The improvement at elevated temperature by 12% TMOS-MgO+Al_2O_3 supports the reasoning that heat transfer in the material should increase with addition of Al_2O_3 *(45)* nanoparticles and that could help achieve better insulation properties at elevated temperature.

During nanocomposite manufacturing, the nanoparticles were mixed using blender. However, it may be possible that the Al_2O_3 and MgO nanoparticles did had their interparticle attraction and didn't mixed well with each other. When the mixed nanoparticles were added to polymer, the dispersion might have worsened further and the pockets of the polymers containing the high concentration of Al_2O_3 or MgO could have formed. Which was also confirmed from the TEM micrographs, wherein the 12% samples had comparatively bigger sizes of agglomerates than the lower loading samples. This can induce the ability of nanocomposite to perform at elevated temperature.

Further to current density, the average electric field stress was measured for all samples at breakdown and plotted (Supporting Information S4). Similar to the trend observed for the current density results, the average electric field stresses at breakdown were found to be 66.72 and 56.8 kV/mm for the 12% TMOS-MgO and 12% TMOS-MgO+Al_2O_3 samples, respectively.

The temperature affected the electrical insulating properties of all samples at different scale. The increase in temperature causes different types of failure mechanism such as the thermal and electromechanical degradation *(46)*. Addition of nanoparticles create the defects in polymer and improves the breakdown strength. As observed the mobility of charge carriers decreased for all the samples. And the addition of Al_2O_3 nanoparticles decreased the rate of thermal degradation by preventing diffusion paths for oxygen and hence increased the thermal transfer through the material. Such dissipation of the energy decreases the leakage of the current through the material when it is subjected to electric field.

The effects of the nanoparticle concentration on the breakdown strength of the nanocomposite are related to two different aspects. The nanoparticles coated with TMOS bonds strongly to the surrounding polymer matrix and create a barrier at the interfacial layer. The surface functionalisation using TMOS facilitated the dispersion of the nanoparticles in the polymer matrix even at the highest concentration of 12 wt% as seen in the TEM images (Figure S2). The sizes of the agglomerated nanoparticles are not significantly different in 12 wt% sample than the 1wt% sample. The minimum agglomeration size of 30 nm as shown in Table 2 is same for all samples. The maximum agglomeration size in 12wt% sample is 220 nm compared to lowest value of the maximum agglomeration for 3% is 115 nm. This suggests that the agglomerate size in the samples containing highest concentration of nanoparticles is not in micrometre scale. Because of relatively small size of agglomerates present in all samples, it can be deduced that the probability of overlapping of agglomerates is less resulting into the reduction of the percolation pathways facilitating charge transfer. As all samples showed the limited changes in the dispersion state (**Table** 3), the formation of the interconnections between nanoparticle agglomerate were limited in the samples with highest concentration of the nanoparticles which otherwise could have facilitated the charge transfer. Any micro-defects in the sample of the nanocomposite could concentrate the charge locally but high nanoparticle content provided the filler for such defects and might have prevented the charge transfer and electrical tree propagation is also hindered by the obstruction developed due to nanoparticle presence in the LDPE matrix. This is evidenced by the decreasing leakage current density of the nanocomposite samples with increasing content of nanoparticles. Progressive decrease in the current density also showed the increasing breakdown strength of the nanocomposite.

Table 3. Interrelating the simulated interaction radius value with all the electrical measurement findings of each sample for a quick comparison.

Sample	Average Interaction Radius (nm)	Leakage current Density @ RT (mA/mm^2 x10^{-9})	Breakdown strength @ RT (kV/mm)	Leakage current Density @ 90 °C (mA/mm^2 x10^{-9})	Breakdown strength @ 90 °C (kV/mm)
LDPE	n/a	1.99±0.10	37.89±1.25	4.52±0.10	35.20±1.0
1% TMOS-MgO	140.80	0.83±0.15	49.88±1.3	3.95±0.12	51.70±0.8
3% TMOS-MgO	139.21	0.75±0.25	51.72±1.20	3.62±0.05	47.50±2.3
9% TMOS-MgO	86.91	0.48±0.05	61.70±1.50	2.24±0.05	58.25±2.1
12% TMOS-MgO	73.09	0.32±0.05	94.80±1.00	0.35±0.05	66.55±3.5
1% TMOS-MgO+Al_2O_3	149.97	1.68±0.05	47.35±1.50	3.93±0.17	51.72±2.2
3% TMOS-MgO+Al_2O_3	135.40	1.58±0.05	41.50±1.0	4.10±0.05	41.31±2.0
9% TMOS-MgO+Al_2O_3	87.29	1.45±0.03	49.95±1.50	2.75±0.05	43.19±2.1
12% TMOS-MgO+Al_2O_3	71.74	1.02±0.10	49.37±1.60	1.10±0.025	56.60±3.0

Considering the findings of the DSC & TGA along with the improved interparticle interaction as reflected by the interaction radius obtained from the simulated model and the electrical responses of each sample as summarised in Table 3.

Conclusion

The silane coating of nanoparticles improved the dispersion, even at higher weight percent (12 wt%) loading of nanoparticles, which resulted in comparatively lower interaction radius and therefore, the increased sites of electron trapping and low space charge accumulation was observed. Further, higher loading of nanoparticles resulted in marginal increase in the crystallinity compared to that of nanocomposites with lower loading of nanoparticles, however, they exhibited the higher resistance to thermal degradation according to DSC and TGA results. The nanocomposite containing TMOS-MgO showed best response than TMOS-MgO+Al_2O_3 and other samples at elevated and room temperature. There is no unified trend was observed in the leakage current and breakdown strength measurements for TMOS-MgO+Al_2O_3 nanocomposite and interface between MgO and Al_2O_3 was not seen forming and improved insulating properties at high temperature. The breakdown strength of the nanocomposite containing TMOS-MgO+Al_2O_3 have improved but it was still not better than 12% TMOS-MgO nanocomposite. Low interaction ratio combined with metal oxide material type (TMOS-MgO or TMOS-MgO+Al_2O_3) governed the decrease in low leakage current density and high breakdown strength. It can be recommended that 12% TMOS-MgO showed overall superior response, with lowest interaction radius, least leakage current allowance and enhanced breakdown strength at elevated temperature. Hence, the 12% TMOS-MgO sample could be the most suitable choice for HVDC insulation. A composite glass ceramic formation between MgO and Al_2O_3 could achieve desired interfaces and improved insulating properties at elevated temperature.

▪ AUTHOR INFORMATION

Corresponding Author

Ketan Pancholi, https://orcid.org/0000-0001-7662-7764
*Phone: +44-1224-262317. E-mail: k.pancholi2@rgu.ac.uk.

ORCID
Ranjeetkumar Gupta: 0000-0001-5647-0691
James Njuguna: 0000-0001-8055-4457

Notes

The authors declare no conflict of interest.

▪ SUPPORTING INFORMATION

In the supporting information document, details of the method followed for the crystallinity measurement using the DSC data is included in section S1. Further the original SEM and TEM micrographs are also included along with the simulated model snaps for all samples in section S2 and S3 respectively. In section S4, plots of the measured average values of the electric field stress at the breakdown for each sample at room temperature and 90°C temperature are included.

▪ ACKNOWLEDGMENTS

The authors thank Robert Gordon University, OGIC-Scotland and Technip Umbilicals Ltd. for financial support. The authors are also grateful to the staff of School of Engineering (David Howie, Alan Mclean, Alexander Laing, David Smith, Martin Johnstone, Alan Macpherson, Patrick and the EA Team). Also, the staff of the School of Pharmacy at Robert Gordon University for making their facility available for part of this research, in particular we like to thank Laurie Smith, Tracy Willox, Bruce Petrie, Carlos Fernandez, Jenny Macaskill & Kerr Mathews.

REFERENCES

(1) Carbon Trust Cable Burial Risk Assessment Methodology "Guidance for The Preparation of Cable Burial Depth of Lowering Specification". **2015**.

(2) Chen, G.; Hao, M.; Xu, Z.; Vaughan, A.; Cao, J.; Wang, H. Review of High Voltage Direct Current Cables. *Csee J. Power and Ernegy Sys.* **2015**, *1*, 9-21.

(3) Cavallini, A.; Montanari, G.; Palmieri, F. Electrical Measurements of Insulating Materials Used in Oil Filled Hvdc Cables: Paper and Paper-Polypropylene-Paper Laminates. *IEEE International Conference on Dielectric Liquids, 2005. ICDL 2005.* **2005**, 409-412.

(4) Runde, M.; Hegerberg, R.; Magnusson, N.; Ildstad, E.; Ytrehus, T. Cavity Formation in Mass-Impregnated Hvdc Subsea Cables-Mechanisms and Critical Parameters. *IEEE Electr. Insul. Mag.* **2014**, *30*, 22-33.

(5) Wang, S.; Chen, P.; Li, H.; Li, J.; Chen, Z. Improved Dc Performance of Crosslinked Polyethylene Insulation Depending on A Higher Purity. *IEEE Trans. Dielectr. Electr. Insul.* **2017**, *24*, 1809-1817.

(6) Du, B.; Hou, Z.; Li, J. In *A Review of Polypropylene and Polypropylene/Inorganic Nanocomposites for HVDC Cable Insulation;* New Trends in High Voltage Engineering; Intech open: 2018.

(7) Zhou, Y.; Peng, S.; Hu, J.; He, J. Polymeric Insulation Materials for HVDC Cables: Development, Challenges and Future Perspective. *IEEE Trans. Dielectr. Electr. Insul.* **2017**, *24*, 1308-1318.

(8) Liao, R.; Bai, G.; Yang, L.; Cheng, H.; Yuan, Y.; Guan, J. Improved Electric Strength and Space Charge Characterization in Ldpe Composites with Montmorillonite Fillers. *Journal of Nanomaterials* **2013**, *2013*, 2.

(9) Pallon, L.; Hoang, A.; Pourrahimi, A.; Hedenqvist, M. S.; Nilsson, F.; Gubanski, S.; Gedde, U.; Olsson, R. T. The Impact of Mgo Nanoparticle Interface in Ultra-Insulating Polyethylene Nanocomposites for High Voltage Dc Cables. *Journal of Materials Chemistry A* **2016**, *4*, 8590-8601.

(10) Nalwa, H. S. *Handbook of Low and High Dielectric Constant Materials and Their Applications, Two-Volume Set*; Elsevier: **1999,** pp. 533-539, ISBN 9780125139052.

(11) Huang, X.; Jiang, P.; Tanaka, T. A Review of Dielectric Polymer Composites with High Thermal Conductivity. *IEEE Electr. Insul. Mag.* **2011**, *27*, 8-16.

(12) Hosier, I.; Praeger, M.; Vaughan, A.; Swingler, S. Electrical Properties of Polymer Nano-Composites Based on Oxide and Nitride Fillers. *2015 IEEE Electrical Insulation Conference (EIC).* **2015**, 438-441.

(13) Wilson, I. Magnesium Oxide as A High-Temperature Insulant. *IEEE Proceedings A (Physical Science, Measurement and Instrumentation, Management and Education, Reviews)* **1981**, *128*, 159-164.

(14) Murata, Y.; Goshowaki, M.; Reddy, C.; Sekiguchi, Y.; Hishinuma, N.; Hayase, Y.; Tanaka, Y.; Takada, T. Investigation of Space Charge Distribution and Volume Resistivity of Xlpe/Mgo Nanocomposite Material Under Dc Voltage Application. *2008 International Symposium on Electrical Insulating Materials (ISEIM 2008).* **2008**, 502-505.

(15) Al-Harthi, M. A.; Bin-Dahman, O. A.; Rahaman, M., King Fahd University of Petroleum, Nanocomposite films with conducting and insulating surfaces, *U.S. Patent Application 14/877*, 623, **2017**.

(16) Hong, J.; Winberg, P.; Schadler, L.; Siegel, R. Dielectric Properties of Zinc Oxide/Low Density Polyethylene Nanocomposites. *Mater Lett* **2005**, *59*, 473-476.

(17) David, E.; Fréchette, M. Polymer Nanocomposites-Major Conclusions and Achievements Reached So Far. *IEEE Electr. Insul. Mag.* **2013**, *29*, 29-36.

(18) Tanaka, T.; Bulinski, A.; Castellon, J.; Frechette, M.; Gubanski, S.; Kindersberger, J.; Montanari, G. C.; Nagao, M.; Morshuis, P.; Tanaka, Y. Dielectric Properties of Xlpe/Sio2 Nanocomposites Based on Cigre Wg D1. 24 Cooperative Test Results. *IEEE Trans. Dielectr. Electr. Insul.* **2011**, *18*, 1482-1517.

(19) Park, Y.; Kwon, J.; Sim, J.; Hwang, J.; Seo, C.; Kim, J.; Lim, K. Dc Conduction and Breakdown Characteristics of Al2o3/Cross-Linked Polyethylene Nanocomposites for High Voltage Direct Current Transmission Cable Insulation. *Japanese Journal of Applied Physics* **2014**, *53*, 08nl05.

(20) Li, Y.; Huang, X.; Hu, Z.; Jiang, P.; Li, S.; Tanaka, T. Large Dielectric Constant and High Thermal Conductivity in Poly (Vinylidene Fluoride)/Barium Titanate/Silicon Carbide Three-Phase Nanocomposites. *Acs Applied Materials & Interfaces* **2011**, *3*, 4396-4403.

(21) Kapoor, P.; Bhagi, A.; Mulukutla, R.; Klabunde, K. In ***Mixed Metal Oxide Nanoparticles;*** Dekker Encyclopedia Of Nanosciences And Nano Technology; Marcel Dekker Inc: 2004; 2007-2017.

(22) Feldman, D. Polymer Nanocomposite Barriers. *Journal of Macromolecular Science, Part A* **2013**, *50*, 441-448, Doi: 10.1080/10601325.2013.768440.

(23) Cerisuelo, J. P.; Gavara, R.; Hernández-Muñoz, P. Diffusion Modeling In Polymer–Clay Nanocomposites for Food Packaging Applications Through Finite Element Analysis of TEM Images. *J. Membr. Sci.* **2015**, *482*, 92-102.

(24) Gupta, R.; Huo, D.; Pancholi, M.; Njuguna, J.; Pancholi, K. Insulating Polymer Nanocomposites for High Thermal Conduction and Fire Retarding Applications. *Defence and Security Doctoral Symposium.* **2017,** Journal contribution. https://doi.org/10.17862/cranfield.rd.5674951.v1.

(25) Toledo, R. R.; Santoyo, V. R.; Sánchez, D. M.; Rosales, M. M. Effect of Aluminum Precursor on Physicochemical Properties of Al2o3 By Hydrolysis/Precipitation Method. *Nova Scientia* **2018**, *10*, 83-99.

(26) Gupta, R.; Pancholi, K.; De, S., Rulston; Murray, D.; Huo, D.; Droubi, G.; White, M.; Njuguna, J. Effect of Oleic Acid Functionalised Iron Oxide Nanoparticles on Properties of Magnetic Polyamide-6 Nanocomposite *JOM,* **2019**, *71(9), 3119-3128. 1-4*

(27) Gupta, R.; Huo, D.; White, M.; Jha, V.; Stenning, G. B.; Pancholi, K. Novel Method of Healing the Fibre Reinforced Thermoplastic Composite: A Potential Model for Offshore Applications. *Composites Communications* **2019,** 16, 67-78.

(28) Gupta, R.; Pancholi, K.; Prabhu, R.; Pancholi, M.; Huo, D.; Jha, V.; Latto, J. Integrated Self-Healing of The Composite Offshore Structures. *Oceans 2017-Aberdeen.* **2017**, IEEE.

(29) Larkin, P. IR And Raman Spectra—Structure Correlations: Characteristic Group Frequencies. *Infrared and Raman Spectroscopy* **2011**, 73-115.

(30) Knözinger, E.; Jacob, K.; Singh, S.; Hofmann, P. Hydroxyl Groups as IR Active Surface Probes on MgO Crystallites. *Surf. Sci.* **1993**, *290*, 388-402.

(31) Cornu, D.; Guesmi, H.; Krafft, J.; Lauron-Pernot, H. Lewis Acid-Basic Interactions Between Co2 And MgO Surface: DFT And Drift Approaches. *The Journal of Physical Chemistry C* **2012**, *116*, 6645-6654.

(32) Prescott, H. A.; Li, Z.; Kemnitz, E.; Deutsch, J.; Lieske, H. New Magnesium Oxide Fluorides with Hydroxy Groups as Catalysts for Michael Additions. *Journal of Materials Chemistry* **2005**, *15*, 4616-4628.

(33) Li, Y. Y.; Han, K. K.; Lin, W. G.; Wan, M. M.; Wang, Y.; Zhu, J. H. Fabrication of A New MgO/C Sorbent for Co 2 Capture at Elevated Temperature. *Journal of Materials Chemistry A* **2013**, *1*, 12919-12925.

(34) Binsbergen, F. Heterogeneous Nucleation in The Crystallization of Polyolefins: Part 1. Chemical and Physical Nature of Nucleating Agents. *Polymer* **1970**, *11*, 253-267.

(35) High-Tech, H. DSC Measurement of Polyethylene—The Correlation of Polyethylene Density and Melting. **1986**.

(36) Liu, D.; Pourrahimi, A. M.; Pallon, L. K.; Sánchez, C. C.; Olsson, R. T.; Hedenqvist, M. S.; Fogelström, L.; Malmström, E.; Gedde, U. W. Interactions Between A Phenolic Antioxidant, Moisture, Peroxide and Crosslinking By-Products with Metal Oxide Nanoparticles in Branched Polyethylene. *Polym. Degrad. Stab.* **2016**, *125*, 21-32.

(37) Chen, J.; Tang, Z.; Bai, Y.; Zhao, S. Multiferroic and magnetoelectric properties of BiFeO3/Bi4Ti3O12 bilayer composite films. *J. Alloys Compounds* **2016**, *675*, 257-265.

(38) Pandey, J.; Gupta, N. Space charge estimation in epoxy-based nanodielectrics using complementary techniques. *2015 IEEE Conference on Electrical Insulation and Dielectric Phenomena (CEIDP).* **2015**, 499-502.

(39) Hoang, A. T.; Pallon, L.; Liu, D.; Serdyuk, Y. V.; Gubanski, S. M.; Gedde, U. W. Charge transport in LDPE nanocomposites Part I—Experimental approach. *Polymers* **2016**, *8*, 87.

(40) Gutsch, S.; Laube, J.; Hartel, A.; Hiller, D.; Zakharov, N.; Werner, P.; Zacharias, M. Charge transport in Si nanocrystal/SiO2 superlattices. *J. Appl. Phys.* **2013**, *113*, 133703.

(41) Li, Q.; Liu, F.; Yang, T.; Gadinski, M. R.; Zhang, G.; Chen, L. Q.; Wang, Q. Sandwich-structured polymer nanocomposites with high energy density and great charge-discharge efficiency at elevated temperatures. *Proc. Natl. Acad. Sci. U. S. A.* **2016**, *113*, 9995-10000, DOI: 10.1073/pnas.1603792113 [doi].

(42) Li, G.; Zhao, H.; Yang, R.; Tang, J.; Li, C.; Lu, Y. Influence of Zr substitution on structure, electrical and magnetic properties of Bi0. 9Ho0. 1FeO3 ceramics. *Results in Physics* **2019**, *14*, 102489.

(43) Robertson, J. High dielectric constant oxides. *The European Physical Journal-Applied Physics* **2004**, *28*, 265-291.

(44) Cho, D.; Mori, T.; Mizutani, T.; Ishioka, M. Effect of Blending on Electrical Conduction and Breakdown of Low-Density Polyethylene Films with Different Densities. *Japanese Journal of Applied Physics* **2001**, *40*, 206.

(45) Huang, C.; Qian, X.; Yang, R. Thermal Conductivity of Polymers and Polymer Nanocomposites. *Materials Science and Engineering: R: Reports* **2018**, *132*, 1-22.

(46) Mayoux, C. Degradation of Insulating Materials Under Electrical Stress. *IEEE Trans. Dielectr. Electr. Insul.* **2000**, *7*, 590-601.

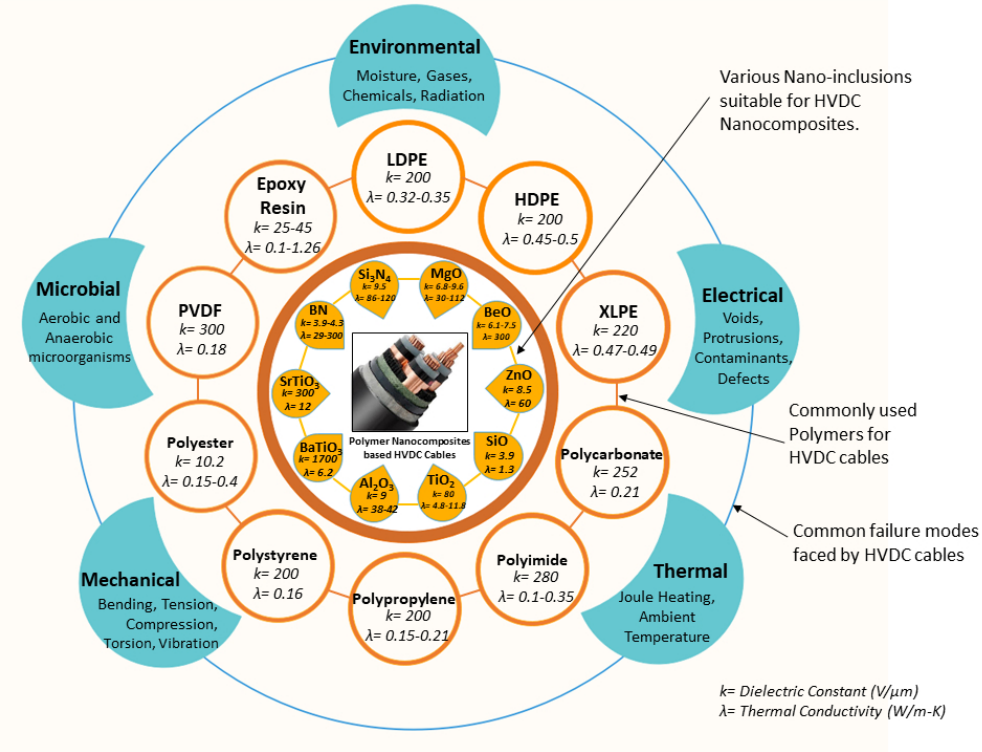

Combinations of nanoparticles and polymers materials to synthesise insulating polymer nanocomposite for the HVDC cables. Associated failure modes of the insulating outer layer is shown in the outermost circle.

252x190mm (96 x 96 DPI)

Supporting Information

Insulating MgO-Al_2O_3-LDPE Nanocomposites for Offshore Medium Voltage DC Cable

Ranjeetkumar Gupta[1,3], Lindsay Smith[2], James Njuguna[1], Alan Deighton[2], Ketan Pancholi[1]*

[1] School of Engineering, Robert Gordon University, Aberdeen AB10 7GE, UK
[2] Technip Umbilicals Ltd., Research and Development Centre, Newcastle upon Tyne, NE6 3PN, UK
[3] Currently at School of Engineering & Physical Sciences, Heriot Watt University, Edinburgh, EH14 4AS, UK
*Correspondence: k.pancholi2@rgu.ac.uk; Tel.: +44-1224-262317.

Section 1 (S1).

The enthalpy of all the samples were calculated using the Universal Analysis software that comes along with the DSC instrument control package. By quantifying the heat associated with the melting endotherm. This heat was then reported in terms of percent crystallinity by normalizing the observed heat of fusion with that of the 100% crystalline LDPE polymer. The area used for the enthalpy (crystallinity) calculation as identified using the "Integrate Peak" functionality of the TA Universal Analysis 2000 software (1) is recreated in the plots in Fig. 6 (included in the main text). The same analysis also helped identify the "Melt Peak Temperature" of the endotherm peak, which was the melting point T_m of the samples and listed in the Table below. Adding to the discussion, the Glass transition temperature T_g was also identified using the "Glass/Step transition" functionality available in the same software.

The degree of crystallinity for all the samples was calculated from the following Equation 1, using the standard reference value of LDPE as cited in the main text.

$$Sample\ Degree\ of\ Crystallinity = \frac{Sample\ Enthalpy\ from\ DSC\ plot}{PA6\ Enthalpy\ from\ Reference\ Text} \times 100\% \qquad \text{Eqn. 1}$$

Section 2 (S2). Original TEM micrographs are shown in Figure S1 and S2.

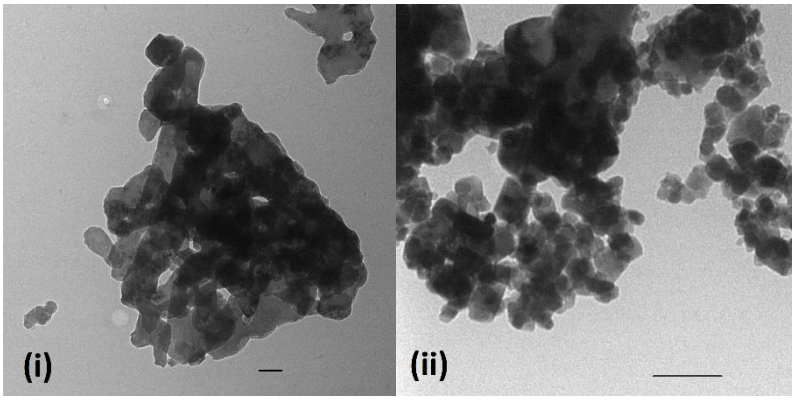

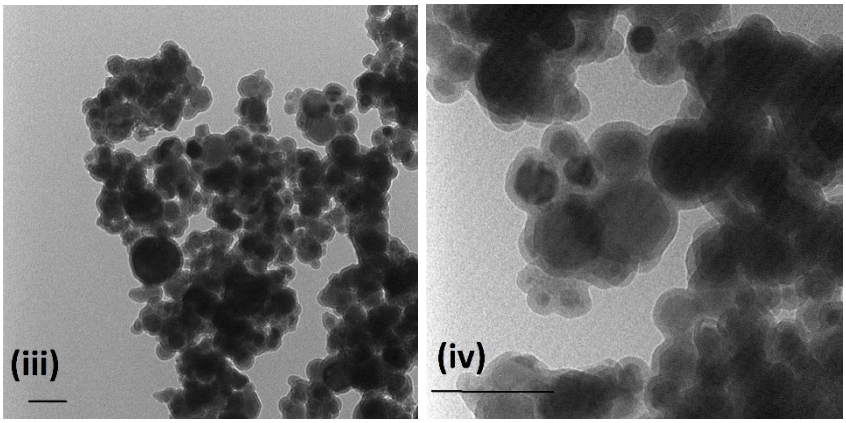

Figure S1. Original TEM images of uncoated [(i) Un-MgO & (ii) Un-Al_2O_3] and coated [(iii) TMOS-MgO & (iv) TMOS-MgO+Al_2O_3] nanoparticles. (Wherein, MgO is assigned as black and Al_2O_3 as red particles respectively, and the Bar Scale marked is of 100 nm)

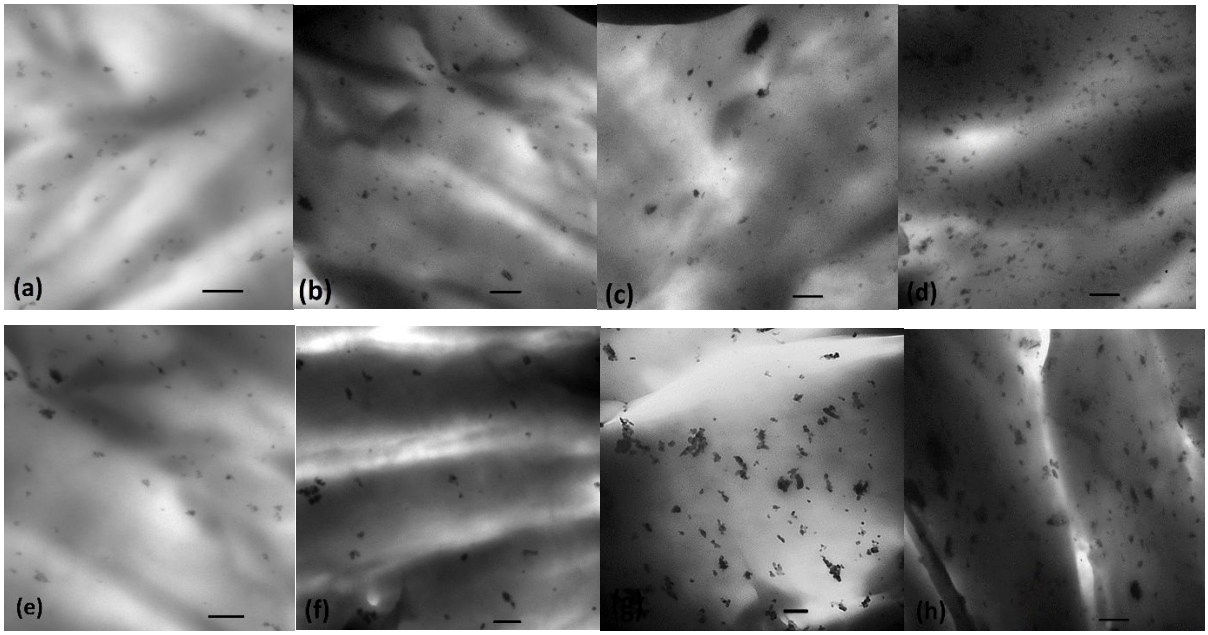

Figure S2. Original TEM micrograph images for samples with MgO variations [(a) 1 wt%, (b) 3 wt%, (c) 9 wt% and (d) 12 wt%] and MgO+Al_2O_3 variations [(e) 1 wt%, (f) 3 wt%, (g) 9 wt% and (h) 12 wt%] of nano-inclusions respectively. (Scale bar shown is of 500 nm)

Section 3 (S3).

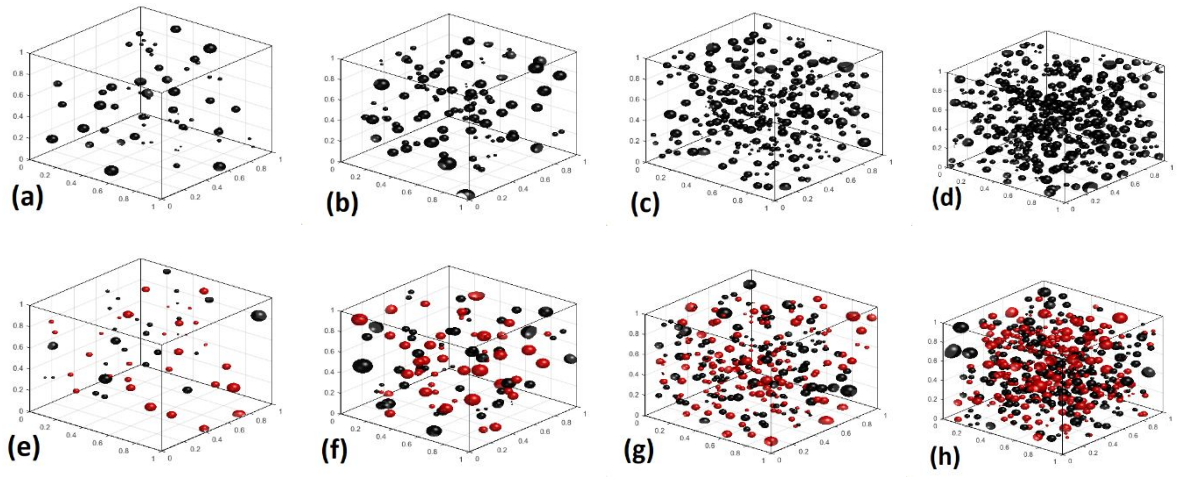

Figure S3. Simulated representation of the synthesised nanocomposites without interaction radius (1 cubic micron size) for MgO variations [(a) 1 wt%, (b) 3 wt%, (c) 9 wt% and (d) 12 wt%] and MgO+Al_2O_3 variations [(e) 1 wt%, (f) 3 wt%, (g) 9 wt% and (h) 12 wt%] of nano-inclusions respectively (Herein, Black spheres represent MgO and Red spheres are for Al_2O_3 nanoparticle or agglomerate respectively.)

The simulated representation of the naoparticle distribution in the synthesised nanocmposite plot without interaction radius is shown in Figure S3.

Section 4 (S4).

The measured average values of the electric field stress at the breakdown for each sample is plotted herein.

The breakdown strength of the materials at room temperature is plotted in Figure S4 and at 90°C temperature in

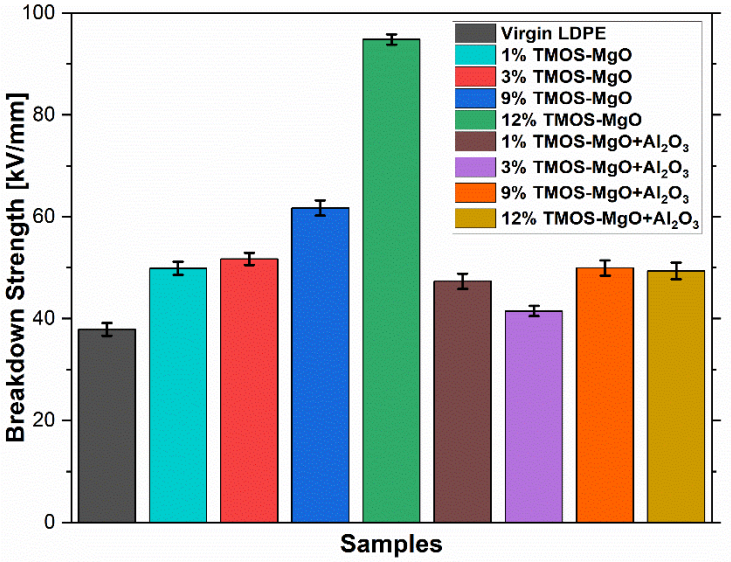

Figure S4. Breakdown strength of all samples at room temperature.

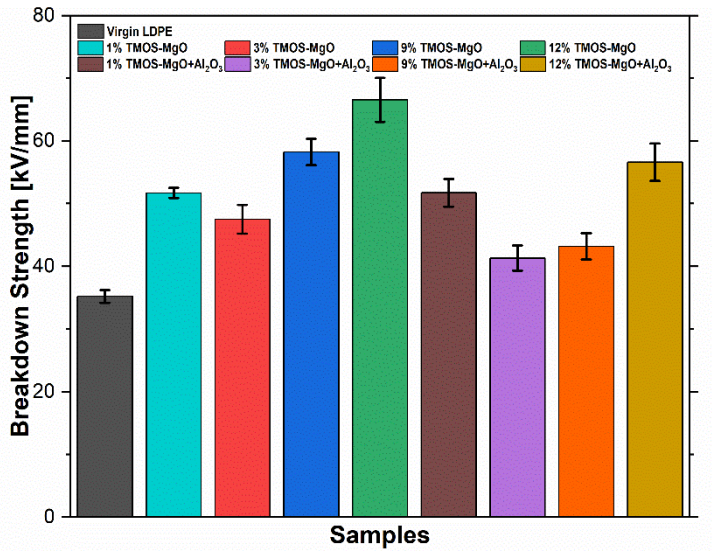

Figure S5. The average electric field stress of the prepared samples at breakdown measured at 90°C.

References

1. Blaine RL. Determination of polymer crystallinity by DSC. TA Instruments, New Castle, DE. 2013.